

A NEURAL SOLVER FOR VARIATIONAL PROBLEMS ON CAD GEOMETRIES WITH APPLICATION TO ELECTRIC MACHINE SIMULATION

Moritz von Tresckow,^{1,*} Stefan Kurz,² Herbert De Gersem,¹ & Dimitrios Loukrezis¹

¹Technische Universität Darmstadt, Institute for Accelerator Science and Electromagnetic Fields, Schlossgartenstr. 8, 64289 Darmstadt, Germany

²University of Jyväskylä, Faculty of Information Technology, Seminaarinkatu 15, Jyväskylä, Finland

*Address all correspondence to: Moritz von Tresckow, Technische Universität Darmstadt, Institute for Accelerator Science and Electromagnetic Fields, Schlossgartenstr. 8, 64289 Darmstadt, Germany, E-mail: moritz.von_tresckow@tu-darmstadt.de

This work presents a deep learning-based framework for the solution of partial differential equations on complex computational domains described with computer-aided design tools. To account for the underlying distribution of the training data caused by spline-based projections from the reference to the physical domain, a variational neural solver equipped with an importance sampling scheme is developed, such that the loss function based on the discretized energy functional obtained after the weak formulation is modified according to the sample distribution. To tackle multi-patch domains possibly leading to solution discontinuities, the variational neural solver is additionally combined with a domain decomposition approach based on the Discontinuous Galerkin formulation. The proposed neural solver is verified on a toy problem and then applied to a real-world engineering test case, namely that of electric machine simulation. The numerical results show clearly that the neural solver produces physics-conforming solutions of significantly improved accuracy.

KEY WORDS: *computer-aided design, domain decomposition, electric machine simulation, neural solvers, numerical simulation, partial differential equations, physics-informed neural networks, variational problems*

1. INTRODUCTION

Recent years have seen a resurgence of numerical methods based on (deep) artificial neural networks (ANNs) for solving ordinary (ODEs) and partial differential equations (PDEs) (Budkina et al., 2016; Chen et al., 2018; E et al., 2017; E and Yu, 2018; Khodayi-Mehr and Zavlanos, 2020; Long et al., 2019, 2018; Mall and Chakraverty, 2016; Raissi et al., 2019; Sirignano and Spiliopoulos, 2018; Yadav et al., 2015). These so-called *neural solvers* revisit an idea with origins more than 20 years ago (Aarts and Van Der Veer, 2001; Dissanayake and Phan-Thien, 1994; Lagaris et al., 1998, 2000; Lee and Kang, 1990; Meade Jr and Fernandez, 1994) in the new light of the ongoing advances in machine learning (ML) technologies, the availability of deep learning

software (Abadi et al., 2016; Al-Rfou et al., 2016; Haghighat and Juanes, 2021; Lu et al., 2021; Paszke et al., 2017), and the capabilities of modern computing hardware (Jouppi et al., 2018; LeCun, 2019). Nevertheless, the use of neural solvers remains limited compared to standard numerical techniques such as the finite element method (FEM) (Hackbusch, 2017; Strang and Fix, 1988). This can be attributed to a number of still unresolved issues, e.g., the lack of theoretical guarantees in terms of convergence and stability (Beck et al., 2019; Shin et al., 2020), or the typically heuristic and often cumbersome procedure of hyperparameter tuning (Kim et al., 2021; Wang et al., 2021). However, there exist problem settings where neural solvers can be advantageous to standard numerical solvers, e.g. considering complex geometries (Berg and Nyström, 2018) or high dimensions (Han et al., 2017; Hutzenthaler et al., 2020).

The core idea behind developing a neural solver is to recast the approximation of an ODE or PDE as an optimization problem, which is the natural setting of ANN training and thus ANN-based approximation. Therein, the main task is to design a suitable loss function, such that the ANN is trained to approximate the solution of the differential equation. Importantly, neural solvers approximate ODE/PDE solutions without having access to solution instants for a set of input data, as in the more common setting of supervised learning. Instead, the loss functions are designed such that the ANN is trained to conform to the physics of the problem described by the differential equation. Several approaches have been proposed in the literature for that purpose. In this work we focus on variational neural solvers for PDEs (E and Yu, 2018; Kharazmi et al., 2021; Khodayi-Mehr and Zavlanos, 2020). In this case, the variational (weak) form of the PDE is first obtained and an ANN is used to approximate the trial functions. Then, the energy functional obtained after the weak form is discretized according to a numerical quadrature rule, e.g. Monte Carlo (MC) or quasi Monte Carlo (QMC) integration (Caffisch et al., 1998; Lemieux, 2009). The discretized energy functional constitutes the loss function to be minimized during model learning, which is typically accomplished with a gradient-based optimization algorithm such as stochastic gradient descent (SGD) (Bottou, 1991) or adaptive moment estimation (ADAM) (Kingma and Ba, 2015). Accordingly, the integration nodes or samples used to discretize the energy functional constitute the training data set. Other approaches construct loss functions based on the strong form of the PDE (Berg and Nyström, 2018; Raissi et al., 2019; Sirignano and Spiliopoulos, 2018). In this case it is often necessary to provide additional methods for the computation of higher-order derivatives, see e.g. (Berg and Nyström, 2018; Sirignano and Spiliopoulos, 2018), as the standard tools of automatic differentiation (AD) (Baydin et al., 2018) might become too cumbersome. In either case, boundary conditions (BCs) are incorporated by imposing hard or soft constraints on the minimization problem (Lagaris et al., 1998; Liao and Ming, 2021; McFall and Mahan, 2009; Raissi et al., 2019).

This work is concerned with the application of variational neural solvers for the solution of PDEs on computational domains described with computer-aided design (CAD) tools, which are commonly employed in engineering design applications. Typically in CAD geometry modeling, B-splines or non-uniform rational B-splines (NURBS) are used to define a projection map from a reference domain to the physical domain, which allows for an exact representation of the geometry (Braibant and Fleury, 1984; Hughes et al., 2005). For complex geometries that cannot be represented by a single transformation of the reference domain in their entirety, a multi-patch approach is typically employed, which corresponds to a decomposition of the domain into non-overlapping subdomains (patches), each of which is represented through a dedicated projection map (Buffa et al., 2015; Langer et al., 2015). In this context, this work aims to address two main problems which arise considering ANN-based PDE approximations on CAD geometries.

The first problem tackled in this work occurs due to the fact that the training data on the

physical geometry must be generated by first sampling the reference domain and then projecting the sampling points onto the physical domain. Then, the projected sampling points follow a distribution dependent on the projection map, which is different than the distribution used to sample the reference domain. This distribution must be taken into account during the discretization of the energy functional, equivalently, for the definition of the loss function. There lies the first contribution of this work, which proposes an importance sampling scheme (Tokdar and Kass, 2010) for discretizing the energy functional, such that the loss function is chosen in accordance to the underlying probability distribution.

The second problem addressed in this work concerns the case of decomposed (multi-patch) CAD geometries, which can possibly lead to sharp changes in the solution, e.g. considering adjacent subdomains with material discontinuities. In this case, it is crucial that the ANN-based approximation is able to resolve the subdomain interface conditions correctly. There lies the second contribution of this work, which proposes a domain decomposition approach along the lines of the Discontinuous Galerkin (DG) method (Brezzi et al., 2000; Cockburn et al., 2012), to be integrated within the variational neural solver. In particular, one ANN is assigned per non-overlapping subdomain and the energy functional is given according to the DG formulation. The corresponding DG-based loss function integrates the contributions from all subdomains, along with additional terms that ensure the satisfaction of the BCs and the interface conditions.

With respect to the latter contribution of this work, we note that recent works have also explored the combination of neural solvers and domain decomposition methods, albeit not in the context of CAD and without making use of the DG method. A shared idea is the use of multiple ANNs, i.e. one per subdomain. In (Li et al., 2019, 2020) the computational domain is partitioned into overlapping subdomains, such that the ANNs are first trained separately and then updated depending on solution agreement on the intersections of the subdomains. Non-overlapping subdomains are used in (Jagtap and Karniadakis, 2020; Jagtap et al., 2020c), where physics-based coupling factors are employed to enforce the interface conditions. An exception to the use of multiple ANNs is the method presented in (Kharazmi et al., 2021), which approximates the PDE with a single ANN, but making use of a separate set of test functions per subdomain. An hp -element-like approximation method based on partition of unity networks is suggested in (Lee et al., 2021; Trask et al., 2021), however, this method concerns a purely data-driven, supervised learning context, where ground truth values are assumed to exist for the function to be approximated, equivalently, for the solution of the PDE. Thus, the variational neural solver proposed in this paper is distinctly different than the ones presented in the aforementioned works.

The neural solver developed in this work is first verified on a toy problem from computational electromagnetics and then applied to a real-world engineering test case, namely, for the simulation of a permanent magnet synchronous machine (PMSM) (Bhat et al., 2018; Bontinck et al., 2018a,b; Ion et al., 2018; Merkel et al., 2021). The real-world test case features all problems that this work aims to address, in particular, a complicated, multi-patch CAD geometry described by means of NURBS, upon which materials with different electromagnetic (EM) properties coexist. Aside from the aforementioned methodological contributions, this is the first time a neural solver is employed to simulate an electric machine, at least to the authors' knowledge.

The rest of this paper is organized as follows. Section 2 details the development of a variational neural solver, using a model problem. Implementation specifics that hold throughout this work are also mentioned in this section. In section 3, the basic tools of CAD geometry representation are presented. In the same section, an importance sampling scheme is derived, which is used to appropriately discretize the energy functional given the projection-dependent sample distribution and accordingly choose the loss function to be minimized during ANN training.

Section 4 considers the case of decomposed CAD domains and further modifies the loss function based on the DG formulation. Numerical experiments which showcase the advantages of the proposed neural solver are available in section 5. A discussion on the findings of the present work as well as a research outlook are available in section 6.

2. VARIATIONAL NEURAL SOLVER

Variational neural solvers are ANN-based approximation methods, which are particularly suited for energy functional minimization problems arising from variational PDE formulations (E and Yu, 2018; Kharazmi et al., 2021; Khodayi-Mehr and Zavlanos, 2020). Postponing the discussion regarding BCs until section 2.4, we consider the elliptic PDE

$$-\Delta u(\mathbf{x}) = f(\mathbf{x}), \quad \mathbf{x} \in \Omega, \quad (2.1)$$

where $\Omega \subset \mathbb{R}^D$ denotes the computational domain and \mathbf{x} is the spatial coordinate vector. Applying the standard tools for the variational formulation (Evans et al., 2012; Hackbusch, 2017), the solution to (2.1) is given by minimizing the energy functional

$$I(u(\mathbf{x})) = \int_{\Omega} \left(\frac{1}{2} |\nabla u(\mathbf{x})|^2 - f(\mathbf{x})u(\mathbf{x}) \right) d\mathbf{x}, \quad (2.2)$$

where u are trial functions living in the Sobolev space $H^1(\Omega)$, and f is a forcing function. Then, the solution of the PDE is given as $u^*(\mathbf{x}) = \operatorname{argmin}_{u \in H^1(\Omega)} I(u(\mathbf{x}))$. In the following, we drop the dependency on the spatial coordinate vector \mathbf{x} wherever possible in order to simplify the notation. The main idea behind variational neural solvers is to train an ANN to minimize the energy functional (2.2), and use this ANN as an approximation to the solution of the PDE, as presented in more detail in sections 2.1 – 2.4.

2.1 ANN-Based Approximation of Trial Functions

The trial functions u in (2.2) are approximated by an ANN, most commonly a multilayer perceptron (MLP). To define the MLP, we must first introduce the concepts of *neuron* and *layer*. A neuron is the smallest unit of an ANN and is mathematically described by the function

$$\mathcal{N}(\mathbf{x}) = \sigma(\mathbf{x}^\top \mathbf{w} + b), \quad (2.3)$$

where $\mathbf{x} \in \mathbb{R}^D$ is the input vector, $\mathbf{w} \in \mathbb{R}^D$ a weight vector, $b \in \mathbb{R}$ a bias term, and $\sigma : \mathbb{R} \rightarrow \mathbb{R}$ a nonlinear function known as the *activation*. A set of neurons which receive the same input form a layer, the output of which is given by

$$\mathcal{L}(\mathbf{x}) = \sigma(\mathbf{x}^\top \mathbf{W} + \mathbf{b}), \quad (2.4)$$

where $\mathbf{W} \in \mathbb{R}^{D \times N}$ is a matrix concatenating the weights of the individual neurons, $\mathbf{b} \in \mathbb{R}^N$ is the corresponding bias vector, and the activation function σ is now applied element-wise for each neuron of the layer. An MLP is a specific type of ANN formed by a sequence of layers and thus described via the layer composition formula

$$\mathcal{MLP}(\mathbf{x}) = \mathcal{L}^{(L)} \left(\mathcal{L}^{(L-1)} \left(\dots \left(\mathcal{L}^{(1)}(\mathbf{x}) \right) \right) \right), \quad (2.5)$$

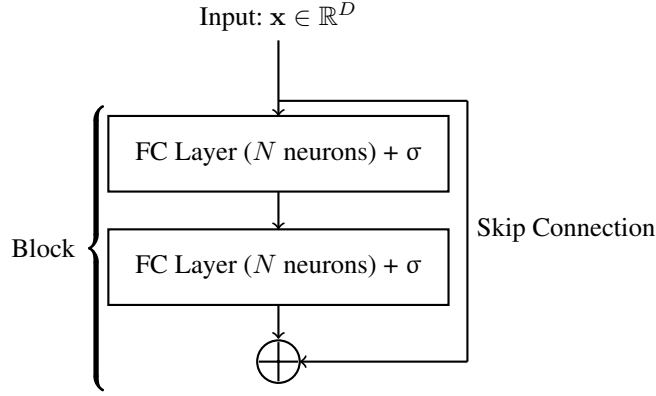


FIG. 1: A single block of the ANN structure employed in this work. We denote with σ the activation function, N is the number of neurons in each fully-connected (FC) layer and \mathbf{x} is the input vector. The output of a block becomes the input of the next block in sequence.

where L denotes the number of layers in sequence. The layers $\mathcal{L}^{(l)}$, $l = 1, \dots, L - 1$, are called the hidden layers and their number defines the depth of the ANN. The weights and biases $\theta = \{\mathbf{W}^{(l)}, \mathbf{b}^{(l)}\}_{l=1}^L$ of the ANN are called the trainable parameters. We denote the approximation of the trial functions by the ANN with $u \approx u_\theta$.

The success of neural solvers, variational or not, depends crucially on ANN architecture, that is, number of layers, layer connection, neurons per layer, and activation functions. The architecture defines the expressive capabilities of the ANN and determines which functions it is able to approximate (Cybenko, 1989; Hornik, 1991). This work adopts the network structure proposed in (E and Yu, 2018), such that the ANNs consist of block sequences, with each block consisting of two fully-connected (FC) layers and a skip connection, see figure 1. The skip connection is used to prevent the so-called vanishing gradient problem (Hochreiter et al., 2001; Pascanu et al., 2013). The number of neurons per FC layer as well as the number of blocks are chosen according to the specific requirements of the application at hand. Additionally, we employ adaptive activation functions of the form $\sigma_l(x) = \tanh(a_l x)$, $l = 1, \dots, L - 1$, where $a_l \in \mathbb{R}$ are layer-based trainable parameters to be optimized along with the weights and biases. The scalable parameters a_l affect the slope of the activation function, which is an important factor regarding the approximation capability of an ANN, and have been found to improve ANN performance in terms of approximation accuracy, robustness, and convergence (Jagtap et al., 2020a,b).

2.2 Energy Functional Discretization and Variational Loss Function

The loss function to be minimized during ANN training is obtained by discretizing the energy functional (2.2) using numerical integration. Accordingly, the quadrature nodes constitute the training data. Most commonly, the energy functional is discretized using pseudo-random samples $\{\mathbf{x}_m\}_{m=1}^M \subset \Omega$, in the spirit of MC or QMC integration (E et al., 2017; Han et al., 2017; Sirignano and Spiliopoulos, 2018), however, Gauss quadrature has also been employed (Kharazmi et al., 2021). The discretization method of choice in this work is QMC sampling based on Sobol

sequences (Cafisch et al., 1998; Lemieux, 2009), hence, the discretized energy functional under the uniform sampling assumption reads

$$I(u) \approx I(u_\theta) \approx \tilde{I}(u_\theta) = \frac{1}{M} \sum_{m=1}^M \left(\frac{1}{2} |\nabla u_\theta(\mathbf{x}_m)|^2 - f(\mathbf{x}_m) u_\theta(\mathbf{x}_m) \right). \quad (2.6)$$

Note that the integral estimator (2.6) will be later corrected according to the importance sampling scheme presented in section 3.2, in order to account for sample distributions induced by CAD tools.

2.3 ANN Training and PDE Solution

A gradient-based optimization algorithm is employed to minimize the discretized energy functional (2.6). In this work, we use the ADAM algorithm (Kingma and Ba, 2015), which updates iteratively the parameter vector θ as

$$\theta_{k+1} = \theta_k - \eta \frac{\hat{\mathbf{m}}_{k+1}}{\sqrt{\hat{\mathbf{v}}_{k+1} + \epsilon}}, \quad (2.7)$$

where $\eta \in \mathbb{R}$ is the learning rate, $\hat{\mathbf{m}}_{k+1}$ the bias-corrected first moment estimate, $\hat{\mathbf{v}}_{k+1}$ the bias-corrected second moment estimate, and $\epsilon > 0$ a small scalar that prevents division by zero. All operations in (2.7) are performed element-wise. The initial values of the ANN's parameter vector θ are obtained using the so-called Xavier initialization (Glorot and Bengio, 2010). Note that the computation of the gradients with respect to either the spatial coordinates or the trainable parameters of the ANN can be performed by means of AD, typically using the backpropagation algorithm (Baydin et al., 2018; Goodfellow et al., 2016). Further note that no mini-batching is employed in this work, i.e. the full training data set is used in every iteration of the ADAM algorithm. Hence, we refer to a single iteration k in (2.7) as an ‘‘epoch’’, which is the standard term used in ML literature to indicate the number of passes of the entire training dataset completed by the training algorithm. The approximate minimizer of (2.2) is obtained by the ANN u_{θ^*} which fulfills

$$\tilde{I}(u_{\theta^*}) \leq \tilde{I}(u_\theta), \quad \forall \theta \in \mathbb{R}^{|\theta|}, \quad (2.8)$$

where $|\theta|$ denotes the dimension of the parameter vector. The overall optimization problem can be summarized to:

$$\text{Find } \theta^* \in \underset{\theta \in \mathbb{R}^{|\theta|}}{\text{argmin}} \tilde{I}(u_\theta). \quad (2.9)$$

2.4 Inclusion of Boundary Conditions

We now complement the PDE (2.1) with Neumann and Dirichlet BCs, thus obtaining the boundary value problem (BVP)

$$-\Delta u = f, \quad \mathbf{x} \in \Omega, \quad (2.10a)$$

$$u = g_D, \quad \mathbf{x} \in \Gamma_D, \quad (2.10b)$$

$$\mathbf{n}_{\Gamma_N} \cdot \nabla u = g_N, \quad \mathbf{x} \in \Gamma_N, \quad (2.10c)$$

where we assume that the boundary $\partial\Omega$ of the computational domain can be separated into a Neumann boundary Γ_N and a Dirichlet boundary Γ_D , such that $\partial\Omega = \Gamma_D \cup \Gamma_N$ with $\Gamma_D \cap \Gamma_N = \emptyset$, and \mathbf{n}_{Γ_N} denotes the outer normal vector on Γ_N .

Neumann BCs are naturally present in the variational formulation, simply modifying the energy functional as

$$I(u) = \int_{\Omega} \left(\frac{1}{2} |\nabla u|^2 - fu \right) d\mathbf{x} - \int_{\Gamma_N} u g_N d\mathbf{x}. \quad (2.11)$$

Thus, Neumann BCs do not have to be explicitly accounted for, other than using separate sets of integration samples within Ω and on Γ_N in the discretization of (2.11), such that

$$I(u_{\theta}) \approx \frac{1}{M} \sum_{m=1}^M \left(\frac{1}{2} |\nabla u_{\theta}(\mathbf{x}_m)|^2 - f(\mathbf{x}_m) u_{\theta}(\mathbf{x}_m) \right) - \frac{1}{J} \sum_{j=1}^J u_{\theta}(\mathbf{x}_j) g_N(\mathbf{x}_j), \quad (2.12)$$

where $\{\mathbf{x}_m\}_{m=1}^M \subset \Omega$ and $\{\mathbf{x}_j\}_{j=1}^J \subset \Gamma_N$.

On the contrary, Dirichlet BCs must be handled separately, as they impose constraints to the space of trial functions u . In this work we use the option of soft constraints for including Dirichlet BCs, in which case a penalty term is added to the energy functional (2.11), forcing the ANN to learn the Dirichlet BCs along with the PDE and the Neumann BCs (Liao and Ming, 2021; Raissi et al., 2019). The modified energy functional reads

$$I(u) = \int_{\Omega} \left(\frac{1}{2} |\nabla u|^2 - fu \right) d\mathbf{x} - \int_{\Gamma_N} u g_N d\mathbf{x} + \beta_D \int_{\Gamma_D} (u - g_D)^2 d\mathbf{x}, \quad (2.13)$$

where β_D is a scalar penalty factor. Similar to the Neumann case, (2.13) must be discretized using different integration samples in Ω , on Γ_N , and on Γ_D , such that

$$\begin{aligned} I(u_{\theta}) \approx & \frac{1}{M} \sum_{m=1}^M \left(\frac{1}{2} |\nabla u_{\theta}(\mathbf{x}_m)|^2 - f(\mathbf{x}_m) u_{\theta}(\mathbf{x}_m) \right) - \frac{1}{J_1} \sum_{j_1=1}^{J_1} u_{\theta}(\mathbf{x}_{j_1}) g_N(\mathbf{x}_{j_1}) \\ & + \beta_D \frac{1}{J_2} \sum_{j_2=1}^{J_2} (u_{\theta}(\mathbf{x}_{j_2}) - g_D(\mathbf{x}_{j_2}))^2, \end{aligned} \quad (2.14)$$

where $\{\mathbf{x}_m\}_{m=1}^M \subset \Omega$, $\{\mathbf{x}_{j_1}\}_{j_1=1}^{J_1} \subset \Gamma_N$, and $\{\mathbf{x}_{j_2}\}_{j_2=1}^{J_2} \subset \Gamma_D$.

3. CAD GEOMETRY REPRESENTATION AND IMPORTANCE SAMPLING

Geometry representation in CAD is typically based on free-form curves, such that the computational domain is defined through a projection map from a reference domain to the physical domain. Central to this procedure are B-splines and NURBSs, presented in more detail in section 3.1. Exactly due to this projection map, a standard MC or QMC discretization of the energy functional, e.g. as in the integral estimator (2.6), is not sufficient, due to the fact that the map induces a sample distribution on the physical domain which is different than the sample distribution on the reference domain. To alleviate this issue, we propose to discretize the energy functional using an importance sampling scheme, such that the loss function takes into account the sample distribution, as shown in section 3.2.

3.1 B-Splines and NURBS

Assuming a *knot vector* $\Xi = \{\xi_1, \dots, \xi_{n+p+1}\} \subset [0, 1]$ such that $\xi_1 \leq \xi_2 \leq \dots \leq \xi_{n+p+1}$, a basis of n piece-wise polynomial functions of degree p can be defined via the Cox-de-Boor recursion formula (Piegl and Tiller, 1996)

$$B_{i,p}(\xi) = \frac{\xi - \xi_i}{\xi_{i+p} - \xi_i} B_{i,p-1}(\xi) + \frac{\xi_{i+p+1} - \xi}{\xi_{i+p+1} - \xi_{i+1}} B_{i+1,p-1}(\xi), \quad i = 1, \dots, n. \quad (3.1)$$

The functions defined by formula (3.1) are called *B-splines*. For $p = 0$, a B-spline is defined as

$$B_{i,0}(\xi) = \begin{cases} 1, & \text{if } \xi_1 \leq \xi < \xi_{i+1}, \\ 0, & \text{otherwise.} \end{cases} \quad (3.2)$$

NURBS can be considered as a generalization of B-splines and are defined through the relation

$$N_{i,p} = \frac{w_i B_{i,p}(\xi)}{\sum_{j=1}^n w_j B_{j,p}(\xi)}, \quad (3.3)$$

where w_i are positive weight factors. Using n NURBS as basis functions along with n control points $\{\mathbf{P}_i\}_{i=1}^n \subset \Omega$, a NURBS curve can be defined as

$$\mathbf{C}(\xi) = \sum_{i=1}^n \mathbf{P}_i N_{i,p}(\xi). \quad (3.4)$$

NURBS surfaces can be created by tensor products of NURBS curves. Using these constructions, it is possible to define a smooth map

$$F : [0, 1]^d \rightarrow \bar{\Omega} \subset \mathbb{R}^d, \quad d \in \{1, 2, 3\}, \quad (3.5)$$

which parametrizes the physical geometry $\bar{\Omega} = \Omega \cup \partial\Omega$. If $\bar{\Omega}$ is not a self-penetrating domain, F is a bijective map (Kleiss and Tomar, 2015). A crucial advantage is that the map F can be easily obtained from any CAD software.

3.2 Importance Sampling-Based Energy Functional Discretization

We consider again the model problem (2.1), where we now assume that the (open-boundary) physical domain Ω is described via a map $F : [0, 1]^2 \rightarrow \Omega$, as in section 3.1. The generation of samples on the physical domain proceeds in two steps. First, uniformly distributed sample points are generated on the unit square, such that $\{\mathbf{y}_m\}_{m=1}^M \subset [0, 1]^2$. Then, the map F is used to project these sample points on the physical geometry, i.e. $F(\{\mathbf{y}_m\}_{m=1}^M) = \{\mathbf{x}_m\}_{m=1}^M \subset \Omega$.

On the physical domain Ω , the sample points are not uniformly distributed, but instead have an underlying distribution which is dependent on the map F . We denote the corresponding probability density function (PDF) with $p(\mathbf{x})$. To derive an explicit expression for $p(\mathbf{x})$, we apply the transformation theorem for PDFs under diffeomorphisms (Klenke, 2006). The theorem states that, for a random vector $\mathbf{y} = (y_1, \dots, y_n)$ with PDF $p_{\mathbf{y}}(\mathbf{y})$ and a diffeomorphism $f : \mathbb{R}^n \rightarrow \mathbb{R}^n$, the PDF $p_{\mathbf{x}}$ of $\mathbf{x} = f(\mathbf{y})$ is given by

$$p_{\mathbf{x}}(\mathbf{x}) = p_{\mathbf{y}}(f^{-1}(\mathbf{x})) \underbrace{\left| \frac{\partial(y_1, \dots, y_n)}{\partial(x_1, \dots, x_n)} \right|}_{:= \Phi_{f^{-1}}}, \quad (3.6)$$

where $\Phi_{f^{-1}}$ is the Jacobian determinant of f^{-1} . The map F is bijective and smooth, therefore, it constitutes a diffeomorphism, is invertible, and the Jacobian of the inverse exists. The bijectivity property holds if the considered domain is not self-penetrating (Kleiss and Tomar, 2015). Since F is bijective, we also know that $F^{-1}(\mathbf{x}_m) \in [0, 1]^2, \forall \mathbf{x}_m, m = 1, \dots, M$. Thus, the PDF $p(\mathbf{x})$ is given as

$$p(\mathbf{x}) = \underbrace{p_{\mathbf{y}}(F^{-1}(\mathbf{x}))}_{=1} \left| \frac{\partial(y_1, \dots, y_n)}{\partial(x_1, \dots, x_n)} \right| = \left| \frac{\partial(y_1, \dots, y_n)}{\partial(x_1, \dots, x_n)} \right| = \Phi_{F^{-1}}(\mathbf{y}). \quad (3.7)$$

An importance sampling-based integral estimator can then be derived as

$$\int_{\Omega} u(\mathbf{x}) d\mathbf{x} \approx \frac{1}{M} \sum_{m=1}^M \frac{u(\mathbf{x}_m)}{p(\mathbf{x}_m)} = \frac{1}{M} \sum_{m=1}^M u(\mathbf{x}_m) \Phi_F(\mathbf{x}_m), \quad (3.8)$$

where the relation $\Phi_{F^{-1}} = (\Phi_F)^{-1}$ is used. Accordingly, the discretized energy functional (2.6) is modified to

$$\tilde{I}(u_{\theta}) = \frac{1}{M} \sum_{m=1}^M \Phi_F(\mathbf{x}_m) \left(\frac{1}{2} |\nabla u_{\theta}(\mathbf{x}_m)|^2 - f(\mathbf{x}_m) u_{\theta}(\mathbf{x}_m) \right). \quad (3.9)$$

The discretization of domain boundaries, e.g. considering the BVP (2.10), proceeds analogously, hence, we omit the explicit form of the discretized energy functional including BCs. Effectively, using the importance sampling scheme for discretizing the energy functional, the terms of the loss function are weighted according to the underlying sample distribution induced by the projection map F .

4. DOMAIN DECOMPOSITION AND DISCONTINUOUS GALERKIN FORMULATION

4.1 Multi-Patch CAD Geometries and Domain Decomposition

In most practical applications, the geometry cannot be parametrized using a single projection map from the reference domain to the physical domain. In such cases, a multi-patch parameterization is employed, which essentially decomposes the computational domain Ω into non-overlapping subdomains $D_k, k = 1, \dots, K$, such that $\Omega = \bigcup_{k=1}^K D_k$. We denote the boundary of each subdomain with ∂D_k . The interface between two adjacent subdomains D_k and D_l is denoted as $\Gamma_{k,l} = \Gamma_{l,k} = \partial D_k \cap \partial D_l$. Assuming that the boundary $\partial\Omega$ consists of a Neumann boundary $\Gamma_N \subset \partial\Omega$ and a Dirichlet boundary $\Gamma_D \subset \partial\Omega$, if part of ∂D_k happens to be on Γ_N or on Γ_D , we denote this part as $\Gamma_{k,N} = \Gamma_k \cap \Gamma_N$ or $\Gamma_{k,D} = \Gamma_k \cap \Gamma_D$, respectively.

For such cases, instead of using a single ANN to approximate the PDE solution over the whole computational domain Ω , we propose to train one ANN per subdomain D_k and then combine the individual subdomain solutions in order to get the solution over the whole domain. However, allowing complete independence between the subdomain-specific ANNs could possibly result in nonphysical solutions, in particular ones that disregard interface conditions to be satisfied on $\Gamma_{k,l}$. For that reason, it is necessary to modify the energy functional in order to account for the interface conditions as well. To that end, methods using physics-based coupling factors and penalty terms have been suggested in the literature (Jagtap and Karniadakis, 2020; Jagtap et al., 2020c). In this work, we propose an alternative approach based on the DG method, which is presented in section 4.2.

4.2 Energy Functional based on the Discontinuous Galerkin Formulation

Focusing on the model BVP (2.10) and assuming a decomposition of the domain Ω as presented in section 4.1, the energy functional is modified along the lines of a DG formulation, such that both BCs and interface conditions are described with average and jump operators (Brezzi et al., 2000; Cockburn et al., 2012). The average operator on u and ∇u is defined as

$$\{u\}_\Gamma = \frac{1}{2}(u_k + u_l), \quad \Gamma \equiv \Gamma_{k,l}, \quad (4.1a)$$

$$\{u\}_\Gamma = g_D, \quad \Gamma \equiv \Gamma_{k,D}, \quad (4.1b)$$

$$\{u\}_\Gamma = u_k, \quad \Gamma \equiv \Gamma_{k,N}, \quad (4.1c)$$

$$\{\nabla u\}_\Gamma = \frac{1}{2}(\nabla u_k + \nabla u_l), \quad \Gamma \equiv \Gamma_{k,l}, \quad (4.1d)$$

$$\{\nabla u\}_\Gamma = \nabla u_k, \quad \Gamma \equiv \Gamma_{k,D}, \quad (4.1e)$$

$$\{\nabla u\}_\Gamma \cdot \mathbf{n}_\Gamma = g_N, \quad \Gamma \equiv \Gamma_{k,N}, \quad (4.1f)$$

where \mathbf{n}_Γ denotes the outer unit normal vector of Γ . The jump operator is defined as

$$[u]_\Gamma = \begin{cases} (u_k - u_l) \cdot \mathbf{n}_\Gamma, & \Gamma \equiv \Gamma_{k,l}, \\ 0, & \Gamma \equiv \Gamma_{k,N}, \\ u_k \cdot \mathbf{n}_\Gamma & \Gamma \equiv \Gamma_{k,D}. \end{cases} \quad (4.2)$$

Using the average and jump operators, the energy functional is modified to

$$\begin{aligned} I(u) &= \sum_{k=1}^K \int_{D_k} \left(\frac{1}{2} |\nabla u_k|^2 - f u_k \right) dx - \sum_{k=1}^K \int_{\Gamma_{k,N}} u_k g_N dx \\ &\quad - \sum_{k=1}^K \sum_{l>k}^K \int_{\Gamma_{k,l}} \{\nabla u\}_{\Gamma_{k,l}} [u]_{\Gamma_{k,l}} dx + \sum_{k=1}^K \sum_{l>k}^K \frac{\beta_{k,l}}{2} \int_{\Gamma_{k,l}} [u]_{\Gamma_{k,l}}^2 dx \\ &\quad - \sum_{k=1}^K \int_{\Gamma_{k,D}} \{\nabla u\}_{\Gamma_{k,D}} [u]_{\Gamma_{k,D}} dx + \sum_{k=1}^K \frac{\beta_{k,D}}{2} \int_{\Gamma_{k,D}} [u - g_D]_{\Gamma_{k,D}}^2 dx, \end{aligned} \quad (4.3)$$

the discretization of which yields the loss function to be minimized during model training. For the discretization of the DG-based energy functional (4.3), we use the importance sampling scheme derived in section 3.2, which shall now be employed per subdomain D_k , $k = 1, \dots, K$. Accordingly, subdomain-specific projection maps $F_k : [0, 1]^2 \rightarrow D_k$ and PDFs $p_k(\mathbf{x})$ are used.

5. NUMERICAL RESULTS

In the following, the variational neural solver developed in this work is first verified on a toy EM field problem and then applied for the purpose of electric machine simulation. In both test cases, the DG-based variational neural solver is compared against a neural solver employing a single ANN, i.e. without any domain decomposition considerations, as well as against a domain decomposition approach which also utilizes one ANN per subdomain along with physics-inspired coupling factors to accommodate the interface conditions, similar to (Jagtap and Karniadakis, 2020; Jagtap et al., 2020c).

In the latter approach, the coupling factors are implemented as additional penalty terms to the energy functional. Revisiting the model BVP (2.10) under the domain decomposition assumptions given in section 4.1, the modified energy functional reads

$$\begin{aligned}
I(u) = & \sum_{k=1}^K \int_{D_k} \left(\frac{1}{2} |\nabla u_k|^2 - fu \right) dx - \sum_{k=1}^K \int_{\Gamma_{k,N}} u_k g_N dx \\
& + \sum_{k=1}^K \beta_{k,D} \int_{\Gamma_{k,D}} (u_k - g_D)^2 dx + \sum_{k=1}^K \sum_{l>k}^K \beta_{k,l} \int_{\Gamma_{k,l}} h_{k,l}(u_k, u_l) dx, \quad (5.1)
\end{aligned}$$

where $h_{k,l}(u_k, u_l)$ are coupling functions imposing a physics-conforming behavior of the combined solution along the interfaces $\Gamma_{k,l}$. The form of the coupling functions is problem-dependent and must be chosen according to the physics governing the problem under investigation. For example, assuming that the solution must be continuous along the interface $\Gamma_{k,l}$, an appropriate choice would be $h_{k,l}(u_k, u_l) = (u_k - u_l)^2$.

Implementation specifics are provided for the employed neural solvers in both test cases, in particular regarding ANN architecture (number of blocks as in figure 1, neurons per layer), learning rates, penalty terms, and training data inside the computational domain and on its boundary. We note that the reported values have been selected using a heuristic procedure, namely an initial grid search followed by manual fine-tuning, and that only the best-in-class configurations are presented. An extensive study with respect to optimizing ANN architecture and the hyperparameters, while definitely interesting and valuable, is out of scope for the present work. For the single-ANN neural solver, the architecture is always chosen such that the trainable parameters are slightly more than those of the multi-ANN neural solvers. With this choice we aim to underline the limited approximation capabilities of the single-ANN approach, even if the employed architecture is comparatively more expressive. Finally, we note that the importance sampling scheme presented in section 3.2 is employed to discretize the energy functional in all cases, as the computational domains are constructed by means of CAD and a naive discretization of the energy functional leads to completely inaccurate results.

5.1 Verification Example: Dielectric Cylinder in Homogeneous Electric Field

As a first test case, we consider the setting of an infinitely long dielectric cylinder suspended in a homogeneous electric field. The geometry is shown in figure 2, where the problem is reduced to a two-dimensional cut due to translational invariance along the z -axis. The computational domain is $\Omega = [-1, 1] \times [-1, 1]$ and the cylinder's domain is $\Omega_c = \{ \mathbf{x} = (x, y) \mid \sqrt{x^2 + y^2} \leq r_0 \}$, where $r_0 = 0.5$ is the radius of the cylinder. The dielectric material of the cylinder has the relative scalar permittivity $\epsilon_c = 100$, while outside the cylinder the relative permittivity is $\epsilon_{nc} = 1$. Hence, the computational domain consists of two subdomains with different material properties and the material interface coincides with the cylinder's boundary $\partial\Omega_c$. The homogeneous electric field is given as $\mathbf{e}_\infty = (E_\infty, 0)$, with $E_\infty = 10$. All sizes are expressed in SI units. We further assume Dirichlet BCs on the left and right boundaries of Ω , and Neumann BCs on the top and bottom boundaries of Ω .

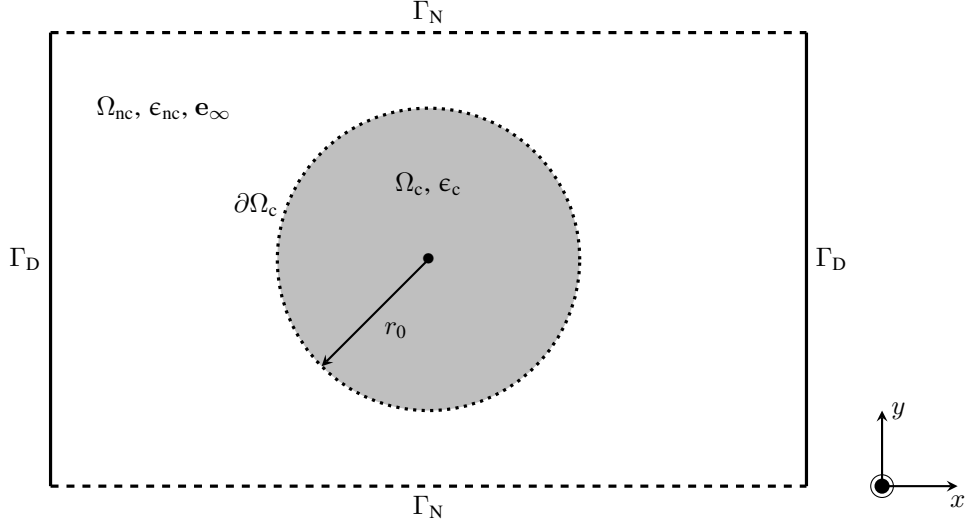


FIG. 2: Two-dimensional cut of a dielectric cylinder suspended in a homogeneous electric field \mathbf{e}_∞ .

The electric potential $u(\mathbf{x})$ in Ω can be computed by solving the BVP

$$-\nabla \cdot (\varepsilon(\mathbf{x}) \nabla u(\mathbf{x})) = 0, \quad \mathbf{x} \in \Omega, \quad (5.2a)$$

$$u(\mathbf{x}) = u^*(\mathbf{x}), \quad \mathbf{x} \in \Gamma_D, \quad (5.2b)$$

$$(\nabla u(\mathbf{x})) \cdot \mathbf{n} = (\nabla u^*(\mathbf{x})) \cdot \mathbf{n}, \quad \mathbf{x} \in \Gamma_N, \quad (5.2c)$$

where \mathbf{n} denotes the outer normal unit vector, the permittivity $\varepsilon(\mathbf{x})$ is given by

$$\varepsilon(\mathbf{x}) = \begin{cases} \varepsilon_c, & \mathbf{x} \in \Omega_c, \\ \varepsilon_{nc}, & \mathbf{x} \in \Omega \setminus \Omega_c, \end{cases} \quad (5.3)$$

and u^* , which is also the analytical solution to the problem, is given by

$$u^*(\mathbf{x}) = -E_\infty x \begin{cases} 1 - \frac{\varepsilon_c/\varepsilon_{nc} - 1}{\varepsilon_c/\varepsilon_{nc} + 1} \frac{r_0^2}{x^2 + y^2}, & \mathbf{x} \in \Omega \setminus \Omega_c, \\ \frac{2}{\varepsilon_c/\varepsilon_{nc} + 1}, & \mathbf{x} \in \Omega_c. \end{cases} \quad (5.4)$$

5.1.1 Energy Functionals

When no domain decomposition is employed, in which case a single ANN approximates the PDE solution over the whole domain, the energy functional to be minimized is

$$\begin{aligned} I(u) = & \int_{\Omega_c} \frac{\varepsilon_c}{2} (\nabla u)^2 d\mathbf{x} + \int_{\Omega \setminus \Omega_c} \frac{\varepsilon_{nc}}{2} (\nabla u)^2 d\mathbf{x} - \int_{\Gamma_N} u \nabla u^* \cdot \mathbf{n} d\mathbf{x} \\ & + \beta_D \int_{\Gamma_D} (u - u^*)^2 d\mathbf{x}. \end{aligned} \quad (5.5)$$

Using one ANN per subdomain in combination with the DG formulation, the energy functional is modified to

$$\begin{aligned}
I(u) = & \int_{\Omega_c} \frac{\epsilon_c}{2} (\nabla u_c)^2 d\mathbf{x} + \int_{\Omega \setminus \Omega_c} \frac{\epsilon_{nc}}{2} (\nabla u_{nc})^2 d\mathbf{x} - \int_{\Gamma_N} u_{nc} \nabla u^* \cdot \mathbf{n} d\mathbf{x} \\
& - \int_{\Gamma_D} \{\nabla u\}_\Gamma [u]_\Gamma d\mathbf{x} + \frac{\beta_D}{2} \int_{\Gamma_D} [u - u^*]_\Gamma^2 d\mathbf{x} \\
& - \int_{\partial\Omega_c} \{\nabla u\}_\Gamma [u]_\Gamma d\mathbf{x} + \frac{\beta_i}{2} \int_{\partial\Omega_c} [u]_\Gamma^2 d\mathbf{x},
\end{aligned} \tag{5.6}$$

where u_c, u_{nc} denote the separate solutions in Ω_c and in $\Omega \setminus \Omega_c$, respectively. Using one ANN per subdomain with coupling factors, we take advantage of the fact that the electric potential must remain continuous, thus, the corresponding energy functional is given by

$$\begin{aligned}
I(u) = & \int_{\Omega_c} \frac{\epsilon_c}{2} (\nabla u_c)^2 d\mathbf{x} + \int_{\Omega \setminus \Omega_c} \frac{\epsilon_{nc}}{2} (\nabla u_{nc})^2 d\mathbf{x} - \int_{\Gamma_N} u_{nc}(\mathbf{x}) \nabla u^*(\mathbf{x}) \cdot \mathbf{n} d\mathbf{x} \\
& + \beta_D \int_{\Gamma_D} (u_{nc} - u^*)^2 d\mathbf{x} + \beta_i \int_{\partial\Omega_c} (u_c - u_{nc})^2 d\mathbf{x}.
\end{aligned} \tag{5.7}$$

5.1.2 Implementation Specifics

When no domain decomposition is employed, the single ANN consists of 6 blocks (see figure 1) with 10 neurons per layer. For both domain decomposition-based neural solvers, the two ANNs consist of 4 blocks with 10 neurons per layer each. For all approaches, we choose a learning rate of $\eta = 1 \cdot 10^{-3}$ for $3 \cdot 10^4$ training epochs, followed by an additional $1 \cdot 10^4$ training epochs where the learning rate $\eta = 1 \cdot 10^{-4}$ is used. The penalty terms are $\beta_i = \beta_D = 1 \cdot 10^3$. The discretization of the energy functionals employs $4 \cdot 10^3$ sample points in Ω , $1.2 \cdot 10^3$ sample points on Γ_D and Γ_N and $6 \cdot 10^2$ sample points on $\partial\Omega_c$.

5.1.3 Simulation Results

Instead of the electric potential, we focus on the static electric field $\mathbf{e} = -\nabla u$. Field continuity demands that, on the interface between the two materials, the tangential field component must remain continuous, i.e. $\mathbf{e}_c^t = \mathbf{e}_{nc}^t$, while the normal field component is discontinuous, i.e. $\mathbf{e}_c^n \neq \mathbf{e}_{nc}^n$. In particular, it must hold that $\epsilon_c \mathbf{e}_c^n = \epsilon_{nc} \mathbf{e}_{nc}^n$, equivalently, $\epsilon_c \nabla u_c \cdot \mathbf{n} = \epsilon_{nc} \nabla u_{nc} \cdot \mathbf{n}$.

Comparisons between ANN-based normal field components \mathbf{e}_θ^n and the analytical one \mathbf{e}_*^n for each neural solver are presented in figure 3. For a better illustration of the results, the normal electric field component is evaluated along the line $y = 0.1$ that cuts the domain Ω horizontally. As can be observed, a single-ANN cannot produce a physics-conforming solution and results in Gibbs' overshooting phenomena that occur exactly on the interface between the two subdomains, i.e. exactly where the material discontinuity exists. The single-ANN seems to have severe approximation difficulties close to the domain boundaries at $x = -1$ and $x = 1$ as well. On the contrary, both domain decomposition-based neural solvers produce physics-conforming solutions that accurately capture the behavior of the electric field's normal component in view of the material discontinuity, as well as close to the domain boundaries. Small approximation difficulties in between the domain boundaries and the material interface can be observed for both methods, however, with evident differences. Given that both neural solvers employ ANNs with

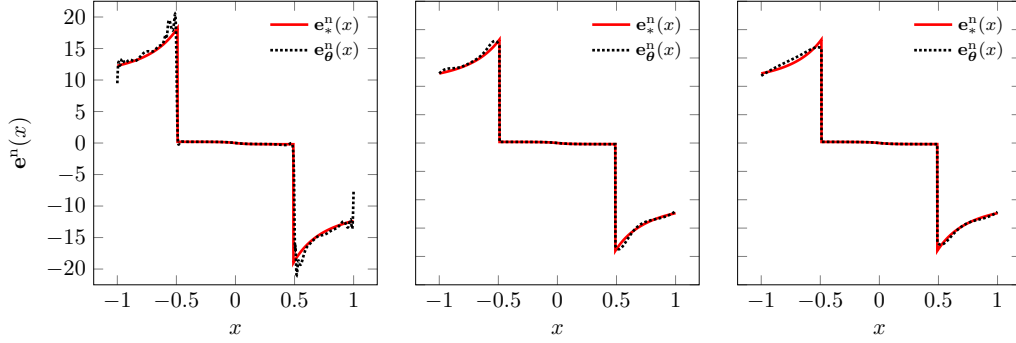


FIG. 3: Normal component of the electric field along the line at $y = 0.1$. Analytically computed field components are denoted with $*$, while θ denotes field components with neural solvers. **Left:** Neural solver based on a single ANN without domain decomposition. **Middle:** Neural solver based on domain decomposition (two ANNs) and the DG formulation. **Right:** Neural solver based on domain decomposition (two ANNs) and coupling factors.

the exact same architecture and hyperparameter values, this result can only be attributed to the different loss functions and their impact upon the training process.

5.2 Engineering Application: Electric Machine Simulation

We now consider a real-world engineering application, namely the simulation of a six-pole PMSM (Bontinck et al., 2018a,b). An illustration is provided in figure 4, where only one-sixth of a two-dimensional cross-section of the PMSM is considered, due to rotational symmetry and translational invariance along the z -axis. The PMSM consists of stator and a rotor, which are separated by an air gap. The rotor consists of an iron part, a permanent magnet, and two air slots connected to the air gap. The stator consists of an iron part and six slots where the copper windings carrying the source current are placed. The air gap is separated into a rotor part and a stator part by the interface Γ_{ag} shown in figure 4. The different material domains are distinguished by the respective magnetic reluctivities, denoted with ν_{Fe} for iron, ν_{Cu} for copper, ν_{PM} for the permanent magnet, and ν_0 for air. The geometry of the PMSM is originally given in 90 non-overlapping patches, 12 for the rotor and 78 for the stator. All patches are described by means of NURBS (Bhat et al., 2018; Merkel et al., 2021). A detailed presentation of the geometrical and material parameters of the PMSM is available in APPENDIX A.

The magnetic field distribution on the PMSM is obtained by the magnetostatic formulation

$$\nabla \times (\nu \nabla \times \mathbf{a}) = \mathbf{j}_{\text{src}} + \nabla \times \mathbf{m}, \quad (5.8)$$

where $\nu = \nu(\mathbf{x}) = \nu(x, y)$ is a piece-wise constant magnetic reluctivity, \mathbf{a} the magnetic vector potential, \mathbf{j}_{src} the source current density, and $\mathbf{m} = (m_x, m_y)$ the magnetization vector of the permanent magnet. We assume that the machine operates in generator mode under no load condition, such that $\mathbf{j}_{\text{src}} = 0$. We additionally assume a constant magnetization in the y -direction, given as $\mathbf{m} = (0, \nu_0 B_r)$, such that the remanent magnetic flux density of the permanent magnet is $\mathbf{b}_{\text{r,PM}} = (0, B_r)$. Under these assumptions, the solution to (5.8) has only a z -component, i.e. $\mathbf{a} = (0, 0, u(\mathbf{x})) = (0, 0, u(x, y))$. We choose anti-periodic BCs on the left and right boundaries of the computational domain and homogeneous Dirichlet BCs on the upper and lower boundaries. We denote the anti-periodic boundary on the left and right hand side of the machine with

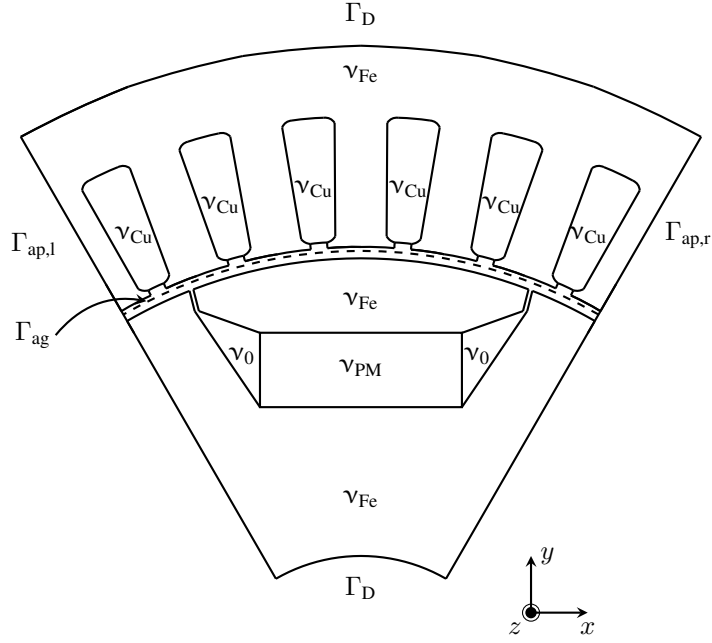


FIG. 4: One-sixth of the PMSM's geometry in two dimensions.

$\Gamma_{ap,l}$ and $\Gamma_{ap,r}$ and the Dirichlet boundary with Γ_D .

5.2.1 Energy Functionals

The assumptions of the PMSM model reduce the PDE (5.8) to a scalar Poisson equation, the energy functional of which is given as

$$I(u) = \frac{1}{2} \int_{\Omega} \nu |\nabla u|^2 d\mathbf{x} - \int_{D_{PM}} \begin{pmatrix} -m_y \\ m_x \end{pmatrix} \cdot \nabla u d\mathbf{x}, \quad (5.9)$$

where D_{PM} denotes the domain of the permanent magnet placed in the rotor. Not considering any domain decomposition, the energy functional on the PMSM is given by

$$\begin{aligned} I(u) = & \frac{1}{2} \int_{\Omega} \nu |\nabla u|^2 d\mathbf{x} + \nu_0 B_r \int_{D_{PM}} \frac{\partial u}{\partial x} d\mathbf{x} \\ & + \beta_D \int_{\Gamma_D} u^2 d\mathbf{x} + \beta_{ap,l} \int_{\Gamma_{ap,l}} (u(x, y) + u(-x, y))^2 d\mathbf{x}. \end{aligned} \quad (5.10)$$

Note that by sampling the anti-periodic boundaries symmetrically, it is sufficient to impose the anti-periodic BCs by integrating along either $\Gamma_{ap,l}$ or $\Gamma_{ap,r}$, where the former is chosen in (5.10).

Turning to the decomposed domain, the DG formulation results in the energy functional

$$\begin{aligned}
I(u) = & \frac{1}{2} \sum_{k=1}^K \int_{D_k} \nu_k |\nabla u_k|^2 \, d\mathbf{x} + \nu_0 B_r \int_{D_{PM}} \frac{\partial u}{\partial x} \, d\mathbf{x} \\
& - \sum_{k=1}^K \sum_{l>k}^K \int_{\Gamma_{k,l}} \{\nabla u_k\}_{\Gamma_{k,l}} [u_k]_{\Gamma_{k,l}} \, d\mathbf{x} + \sum_{k=1}^K \sum_{l>k}^K \frac{\beta_{k,l}}{2} \int_{\Gamma_{k,l}} [u]_{\Gamma_{k,l}}^2 \, d\mathbf{x} \\
& - \int_{\Gamma_D} \{\nabla u\}_{\Gamma_D} [u]_{\Gamma_D} \, d\mathbf{x} + \frac{\beta_D}{2} \int_{\Gamma_D} [u]_{\Gamma_D}^2 \, d\mathbf{x} \\
& - \int_{\Gamma_{ap,1}} \{\nabla u\}_{\Gamma_{ap,1}} [u]_{\Gamma_{ap,1}} \, d\mathbf{x} + \frac{\beta_{ap,1}}{2} \int_{\Gamma_{ap,1}} [u]_{\Gamma_{ap,1}}^2 \, d\mathbf{x},
\end{aligned} \tag{5.11}$$

where the average and jump operators on the left anti-periodic boundary $\Gamma_{ap,1}$ are defined as $\{\nabla u\}_{\Gamma_{ap,1}} = \frac{1}{2}(\nabla u(x, y) + \nabla u(-x, y))$ and $[u]_{\Gamma_{ap,1}} := (u(x, y) + u(-x, y)) \cdot \mathbf{n}_{ap,1}$, respectively. When coupling factors are employed, the corresponding energy functional reads

$$\begin{aligned}
I(u) = & \frac{1}{2} \sum_{k=1}^K \int_{D_k} \nu_k |\nabla u_k|^2 \, d\mathbf{x} + \nu_0 B_r \int_{D_{PM}} \frac{\partial u}{\partial x} \, d\mathbf{x} \\
& + \sum_{k=1}^K \sum_{l>k}^K \beta_{k,l} \int_{\Gamma_{k,l}} h_{k,l}(u_k, u_l) \, d\mathbf{x} + \beta_D \int_{\Gamma_D} u(\mathbf{x})^2 \, d\mathbf{x} \\
& + \beta_{ap,1} \int_{\Gamma_{ap,1}} (u(x, y) + u(-x, y))^2 \, d\mathbf{x},
\end{aligned} \tag{5.12}$$

where $h_{k,l}(u_k, u_l) = (u_k - u_l)^2$, taking advantage of the continuity of the magnetic vector potential.

5.2.2 Implementation Specifics

When no domain decomposition is considered, the single ANN consists of 30 blocks with 24 neurons per hidden layer, thus resulting in 36025 trainable parameters. In the case of the domain decomposition-based neural solvers, instead of using the original patches that form the geometry of the PMSM, we construct subdomains by combining patches with the same material property and allocate a single ANN for each. This yields a material-based domain decomposition which is illustrated in figure 5 and further explained in table 1. Table 1 also provides details regarding the architecture of the ANN assigned to each subdomain, as well as the number of trainable parameters $|\Theta|$ and the size of the training data set N_{sd} per subdomain. The total number of trainable parameters for the DG-based neural solver is 33354. The training data set consists of $63 \cdot 10^3$ sampling points, the distribution of which on the domain of the PMSM is shown in figure 5. For the implementation of the boundary and interface conditions, we use 2800 sampling points on the anti-periodic boundaries, 1100 sampling points on the Dirichlet boundaries, and 13500 sampling points on the subdomain interfaces. The ANNs are trained with the learning rate $\eta = 1 \cdot 10^{-3}$ for 5000 epochs. Last, the penalty factors β_D , $\beta_{k,l}$, and $\beta_{ap,1}$ in (5.11) are equal to either $\beta_{rt} = 1 \cdot 10^5$ or $\beta_{st} = 2 \cdot 10^4$, depending on whether the original patch belongs to the rotor or the stator, respectively.

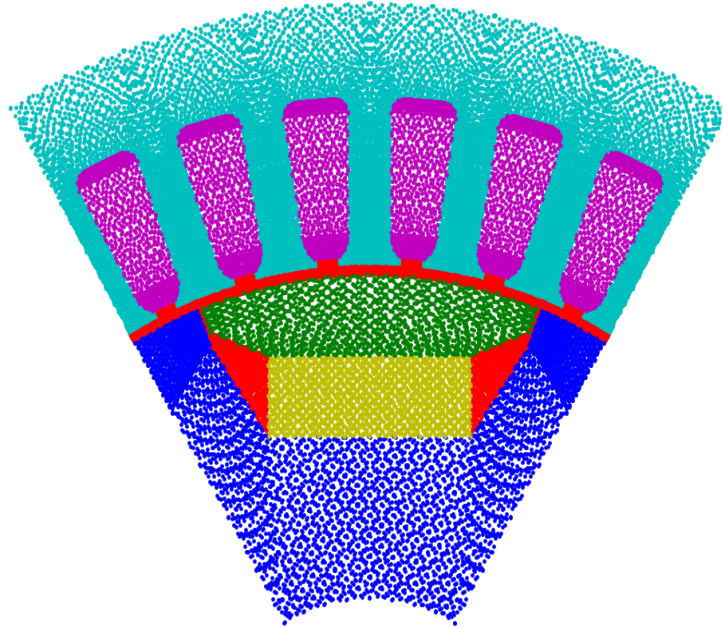


FIG. 5: Domain partitioning and QMC sampling on the geometry of the PMSM.

5.2.3 Simulation Results

Figure 6 shows the magnetic vector potential solutions provided by the three employed neural solvers at the end of the training process, as well as a reference solution obtained with an iso-geometric analysis (IGA)-FEM solver (Bontinck et al., 2018a). It is visually evident that the solution provided by a single ANN differs significantly from the reference, particularly in the regions on the left and right of the permanent magnet (bright yellow and deep blue regions). On the contrary, the solutions provided by both domain decomposition-based neural solvers, i.e.

Subdomain	Color in Fig. 5	Blocks	Neurons per Layer	$ \theta $	$N_{sd}/10^3$
Outer rotor yoke	Green	8	15	3872	2
Inner rotor yoke	Blue	8	15	3872	6
Air Slits/Air Gap	Red	15	15	7246	26
Permanent Magnet	Yellow	8	15	3872	2
Stator Yoke	Cyan	15	15	7246	21
Stator Windings	Magenta	15	15	7246	6

TABLE 1: Domain partitioning and ANN architecture for the domain decomposition-based neural solvers.

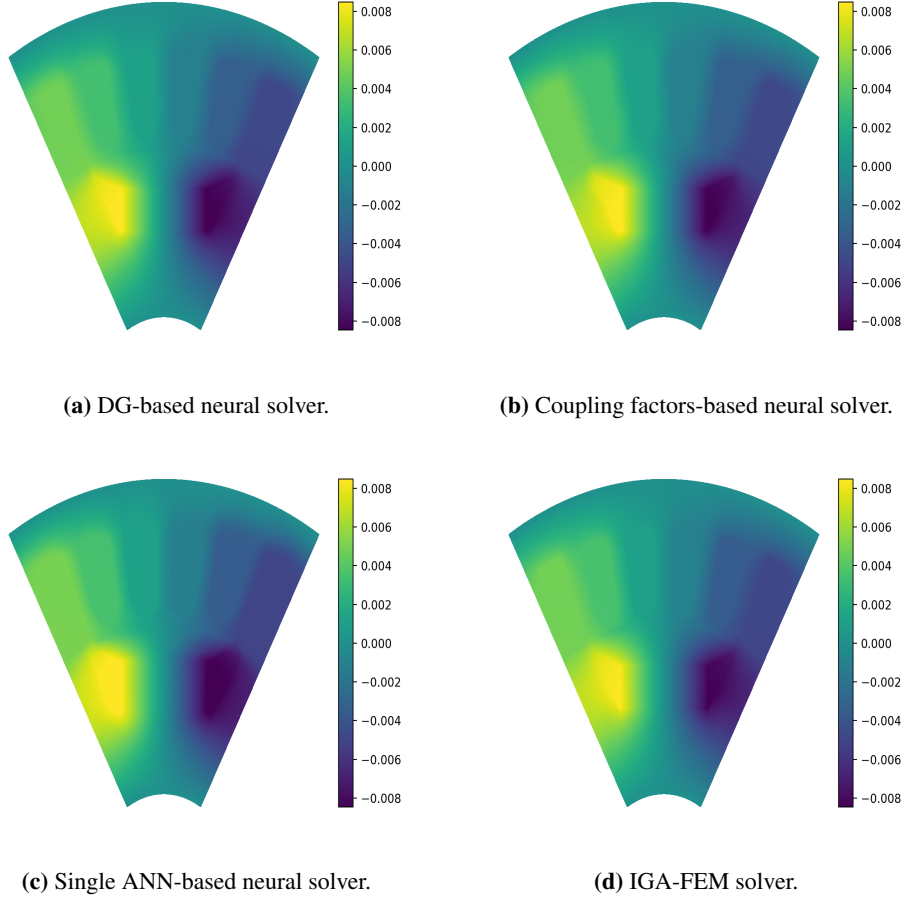


FIG. 6: Solutions of the magnetic vector potential a_z [Vsm^{-1}] using the reference IGA-FEM solver, the neural solver based on a single ANN without domain decomposition, the neural solver utilizing domain decomposition based on the DG formulation, and the neural solver utilizing domain decomposition based on coupling factors.

either based on the DG formulation or on coupling factors, are visually almost identical to the reference.

The differences between the solutions provided by the three neural solvers become more easily distinguishable in figure 7, which shows the absolute error of each ANN-based solution with respect to the reference IGA-FEM over the whole domain of the PMSM. The absolute error is computed using $63 \cdot 10^3$ randomly generated sampling points on the domain of the PMSM, which are not included in the training data. For the DG and coupling factors-based neural solvers, the error remains below $5 \cdot 10^{-4}$ over the whole domain of the PMSM, whereas the single ANN-based approximation yields worst-case errors three times higher. In all three cases, the worst-case errors are concentrated around the corners of the permanent magnet. However, the single ANN-based neural solver results in comparatively high errors in other regions of the PMSM as well, e.g. on the upper parts of the stator.

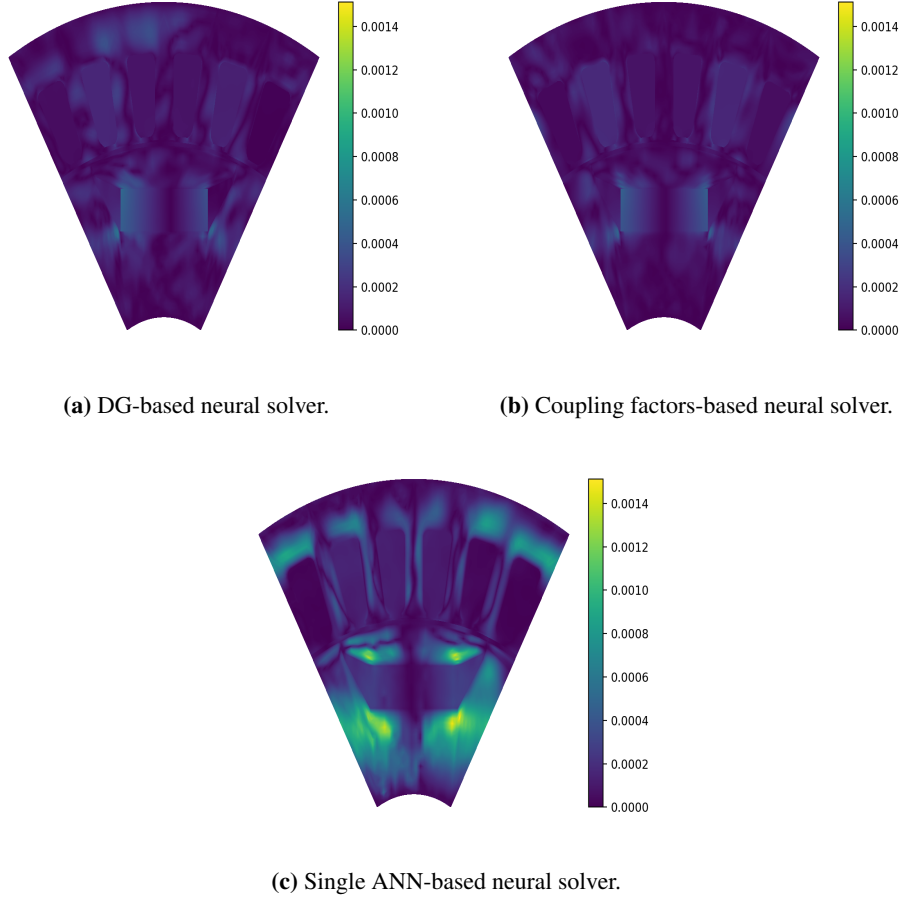


FIG. 7: Absolute errors of the magnetic vector potential solutions provided by the DG-based neural solver, the coupling factors-based neural solver, and the single ANN-based neural solver, with respect to the IGA-FEM reference solution.

In figure 8, we attempt a deeper comparison between the two domain decomposition-based neural solvers. As noted before, both neural solvers yield a maximum absolute error smaller than $5 \cdot 10^{-4}$. We note that the mean absolute and mean squared errors computed over the PMSM's domain are almost identical as well. Nevertheless, it is evident that the error distribution over the PMSM's domain differs significantly. This result is similar to the one observed in section 5.1 and can only be attributed to the different loss functions, given the fact that the ANN architectures and the hyperparameters are identical for both methods.

As a final remark for this study, we note that the reference IGA-FEM model uses non-conforming patches, thus resulting in a discontinuous magnetic vector potential along the interface Γ_{ag} between rotor and stator. Contrarily, all three neural solvers yield a continuous magnetic vector potential within the air gap, which is the correct physical behavior. Nevertheless, this discrepancy has only a minor impact on the computed errors. Here lies a possible advantage of neural solvers over traditional solvers, which merits further investigation.

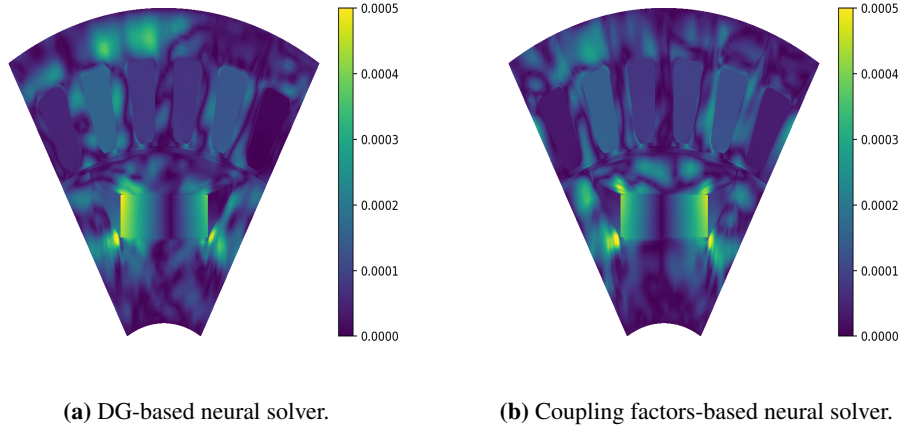


FIG. 8: Comparison between the two domain decomposition-based solvers in terms of the absolute approximation error with respect to the IGA-FEM reference solution.

6. DISCUSSION, CONCLUSION, AND OUTLOOK

In this paper, we presented a novel deep learning-based method for the solution of variational problems, which can be seamlessly integrated into CAD workflows. An importance sampling scheme is employed for the discretization of the energy functional obtained from the variational form of the PDE, which allows to correct the loss function according to the sample distribution on the physical domain induced by CAD tools such as B-splines or NURBS. Complicated, multi-patch CAD domains are addressed by further modifying the loss function based on a decomposition of the computational domain and the DG formulation. Minimizing the DG-based loss function allows the neural solver to produce solutions that satisfy the necessary conditions which must be met on the interfaces between subdomains and thus correctly capture sharp changes in the PDE solution.

The solver developed in this work was verified on two test cases, namely, a toy problem from EM field theory and a real-world engineering application concerning electric machine simulation. Compared to a neural solver utilizing a single ANN, the DG-based neural solver is found to be significantly more accurate. Importantly, the approximations obtained with the DG-based neural solver conform to the physics of each considered test case, which is not always the case when a single ANN is used.

The DG-based neural solver was also compared against a domain decomposition-based approach previously suggested in the literature (Jagtap and Karniadakis, 2020; Jagtap et al., 2020c), which introduces physics-inspired coupling factors and corresponding penalty terms in the loss function. The two domain decomposition-based neural solvers are found to perform comparably well, however, it was observed that the different loss functions result in non-negligible differences in the distribution of the approximation error over the computational domain. These results merit further investigations on the spatial dependency of the approximation accuracy of domain decomposition-based neural solvers, which should be extended to other approaches found in the literature as well, see e.g. (Kharazmi et al., 2021; Li et al., 2019, 2020). We note however that the DG formulation, while not clearly superior to competitive approaches, offers a complete and generally applicable framework for the development of domain decomposition-based neural

solvers, as follows from its extensive application in the context of the FEM.

One drawback of the neural solver proposed in this work, as well as of neural solvers in general, concerns the duration of ANN-based simulation, which is mainly attributed to model training and typically exceeds significantly the simulation times of standard numerical solvers. For example, the IGA-FEM solver which produced the reference solution in section 5.2 was significantly faster than any of the employed neural solvers. We should note that our simulations were performed using standard central processing units (CPUs), whereas more advanced computing equipment such as graphics processing units (GPUs) are typically necessary for achieving a good performance in ANN training. Nevertheless, accelerated model training is necessary for neural solvers to become a truly competitive alternative to traditional numerical simulation methods. In connection to other persisting problems in ANN-based PDE approximation, exemplarily, the lack of convergence and stability theory, the need for hyperparameter fine-tuning, and possible overfitting problems, it should not be expected that neural solvers will replace traditional numerical solvers in the near future. This should not be surprising, as neural solvers have been revitalized only in the last few years, whereas PDE solvers based on the FEM or on other numerical schemes have been continuously developed and optimized for several decades. We note that an extensive discussion on the potential of neural solvers to replace or accelerate traditional numerical solution techniques can be found in (Markidis, 2021).

Nevertheless, there exist problem settings where neural solvers can be advantageous to traditional numerical methods. One relevant case is reported in (Berg and Nyström, 2018), where a traditional mesh-based solver fails due to the complexities of the problem’s geometry, whereas the neural solver is able to provide the solution to the PDE. In the context of this work, in particular regarding the PMSM simulation presented in section 5.2, the numerical results revealed that the neural solvers were able to provide physics-conforming solutions in the challenging domain of the air gap between rotor and stator, where the reference IGA-FEM solver fails to do so due to the use of a non-conforming patches. Motivated by this observation, a promising research direction would be the combination of traditional and neural solvers, each applied to different regions of the computational domain where it is expected to perform better than the other. Another possible problem setting where the utilization of neural solvers could prove to be advantageous would be for the approximation of PDEs with highly nonlinear constitutive (material) laws, which often pose significant problems for standard numerical approximation techniques (Galetzka et al., 2021). Last but not least, neural solvers are known to scale favorably for high-dimensional PDEs (Han et al., 2017; Hutzenthaler et al., 2020), which constitute a common bottleneck for standard numerical techniques. In the context of engineering design, typical settings where high-dimensional PDEs arise include optimization, uncertainty quantification, or parameter inference studies. It can be expected that neural solvers can mitigate the so-called curse of dimensionality and provide insights for these challenging problems.

Last, an important direction for future research concerns the development of neural solvers which preserve important physical quantities. In the context of this work, such physical quantities include continuity relations for electric and magnetic fields at material interfaces, as well as continuity of the electric potential. While these conditions are indeed found to be respected by the ANN-based solutions provided by the neural solver developed in this work, there is no a priori guarantee for that result, due to the fact that a “soft constraints” approach has been employed for ANN training. Such a guarantee could be achieved with the use of hard constraints or similar approach (McFall and Mahan, 2009). In that case, one should refer to the corresponding neural solver as “physics-constrained” rather than “physics-informed”, where the latter term is

more appropriate for the neural solver presented in this paper. Such physics-constrained neural solvers would also compare more favorably against traditional numerical solution methods which indeed guarantee the preservation of physical quantities.

ACKNOWLEDGEMENTS

This work was partially supported by the joint DFG/FWF Collaborative Research Centre CREATOR (CRC/TRR 361, F90) at TU Darmstadt, TU Graz, and JKU Linz.

Dimitrios Loukrezis and Herbert De Gersem are supported by the Graduate School Computational Engineering within the Centre for Computational Engineering at TU Darmstadt.

The authors would like to thank Prof. Dr. rer. nat. Sebastian Schöps and Melina Merkel M.Sc. from the Chair of Computational Electromagnetics (CEM) at TU Darmstadt, as well as the former CEM members Dr.-Ing. Zeger Bontinck and Dr.-Ing. Jacopo Corno, for providing the PMSM geometry data and the corresponding IGA-FEM solver.

REFERENCES

- Aarts, L.P. and Van Der Veer, P., Neural Network Method for Solving Partial Differential Equations, *Neural Processing Letters*, vol. **14**, no. 3, pp. 261–271, 2001.
- Abadi, M., Barham, P., Chen, J., Chen, Z., Davis, A., Dean, J., Devin, M., Ghemawat, S., Irving, G., Isard, M., and others, Tensorflow: A System for Large-Scale Machine Learning, *12th USENIX symposium on operating systems design and implementation (OSDI 16)*, pp. 265–283, 2016.
- Al-Rfou, R., Alain, G., Almahairi, A., Angermueller, C., Bahdanau, D., Ballas, N., Bastien, F., Bayer, J., Belikov, A., Belopolsky, A., and others, Theano: A Python Framework for Fast Computation of Mathematical Expressions, *arXiv e-prints*, pp. arXiv–1605, 2016.
- Baydin, A., Pearlmutter, A., Radul, A., and Siskind, M., Automatic Differentiation in Machine Learning: A Survey, *The Journal of Machine Learning Research*, vol. **18**, no. 1, pp. 1–19, 2018.
- Beck, C., Jentzen, A., and Kuckuck, B., Full Error Analysis for the Training of Deep Neural Networks, *arXiv preprint arXiv:1910.00121*, 2019.
- Berg, J. and Nyström, K., A Unified Deep Artificial Neural Network Approach to Partial Differential Equations in Complex Geometries, *Neurocomputing*, vol. **317**, pp. 28–41, 2018.
- Bhat, P., Bontinck, Z., Corno, J., Schöps, S., and De Gersem, H., Modelling of a Permanent Magnet Synchronous Machine using Isogeometric Analysis, *COMPEL-The international journal for computation and mathematics in electrical and electronic engineering*, 2018.
- Bontinck, Z., Corno, J., Schöps, S., and De Gersem, H., Isogeometric Analysis and Harmonic Stator-Rotor Coupling for Simulating Electric Machines, *Computer Methods in Applied Mechanics and Engineering*, vol. **334**, pp. 40–55, 2018a.
- Bontinck, Z., Lass, O., Schöps, S., De Gersem, H., Ulbrich, S., and Rain, O., Robust Optimisation Formulations for the Design of an Electric Machine, *IET Science, Measurement & Technology*, vol. **12**, no. 8, pp. 939–948, 2018b.
- Bottou, L., Stochastic Gradient Learning in Neural Networks, *Proceedings of Neuro-Nimes*, vol. **91**, no. 8, p. 12, 1991.
- Braibant, V. and Fleury, C., Shape Optimal Design using B-Splines, *Computer methods in applied mechanics and engineering*, vol. **44**, no. 3, pp. 247–267, 1984.

- Brezzi, F., Manzini, G., Marini, D., Pietra, P., and Russo, A., Discontinuous Galerkin Approximations for Elliptic Problems, *Numerical Methods for Partial Differential Equations*, vol. **16**, no. 4, pp. 365–378, 2000.
- Budkina, E.M., Kuznetsov, E.B., Lazovskaya, T.V., Leonov, S.S., Tarkhov, D.A., and Vasilyev, A.N., Neural Network Technique in Boundary Value Problems for Ordinary Differential Equations, *International Symposium on Neural Networks*, Springer, pp. 277–283, 2016.
- Buffa, A., Vázquez, R.H., Sangalli, G., and Beirão da Veiga, L., Approximation Estimates for Isogeometric Spaces in Multipatch Geometries, *Numerical Methods for Partial Differential Equations*, vol. **31**, no. 2, pp. 422–438, 2015.
- Cafisch, R.E. , Monte Carlo and Quasi-Monte Carlo Methods, *Acta numerica*, vol. **1998**, pp. 1–49, 1998.
- Chen, R.T., Rubanova, Y., Bettencourt, J., and Duvenaud, D., Neural Ordinary Differential Equations, *arXiv preprint arXiv:1806.07366*, 2018.
- Cockburn, B., Karniadakis, G.E., and Shu, C.W., *Discontinuous Galerkin Methods: Theory, Computation and Applications*, Vol. 11, Springer Science & Business Media, 2012.
- Cybenko, G., Approximation by Superpositions of a Sigmoidal Function, *Mathematics of Controls, Signals and Systems*, vol. **2**, no. 4, pp. 303–314, 1989.
- Dissanayake, M. and Phan-Thien, N., Neural-Network-Based Approximations for Solving Partial Differential Equations, *Communications in Numerical Methods in Engineering*, vol. **10**, no. 3, pp. 195–201, 1994.
- E, W., Han, J., and Jentzen, A., Deep Learning-Based Numerical Methods for High-Dimensional Parabolic Partial Differential Equations and Backward Stochastic Differential Equations, *Communications in Mathematics and Statistics*, vol. **5**, no. 4, pp. 349–380, 2017.
- E, W. and Yu, B., The Deep Ritz Method: a Deep Learning-Based Numerical Algorithm for Solving Variational Problems, *Communications in Mathematics and Statistics*, vol. **6**, no. 1, pp. 1–12, 2018.
- Evans, G., Blackledge, J., and Yardley, P., *Numerical Methods for Partial Differential Equations*, Springer Science & Business Media, 2012.
- Galetzka, A., Loukrezis, D., and De Gersem, H., Data-Driven Solvers for Strongly Nonlinear Material Response, *International Journal for Numerical Methods in Engineering*, vol. **122**, no. 6, pp. 1538–1562, 2021.
- Glorot, X. and Bengio, Y., Understanding the Difficulty of Training Deep Feedforward Neural Networks, *Proceedings of the thirteenth international conference on artificial intelligence and statistics*, pp. 249–256, 2010.
- Goodfellow, I., Bengio, Y., Courville, A., and Bengio, Y., *Deep Learning*, Vol. 1, MIT press Cambridge, 2016.
- Hackbusch, W., *Elliptic Differential Equations: Theory and Numerical Treatment*, Vol. 18, Springer, 2017.
- Haghighat, E. and Juanes, R., SciANN: A Keras/TensorFlow Wrapper for Scientific Computations and Physics-Informed Deep Learning using Artificial Neural Networks, *Computer Methods in Applied Mechanics and Engineering*, vol. **373**, p. 113552, 2021.
- Han, J., Jentzen, A., and E, W., Solving High-Dimensional Partial Differential Equations using Deep Learning, *Proceedings of the National Academy of Sciences*, vol. **115**, pp. 1–12, 2017.
- Hochreiter, S., Bengio, Y., Frasconi, P., Schmidhuber, J., , Gradient flow in recurrent nets: the difficulty of learning long-term dependencies, , 2001.
- Hornik, K., Approximation Capabilities of Multilayer Feedforward Networks, *Neural Networks*, vol. **4**, no. 2, pp. 251–257, 1991.
- Hughes, T., Cottrell, J., and Bazilevs, Y., Isogeometric Analysis: CAD, Finite Elements, NURBS, Exact Geometry and Mesh Refinement, *Computer methods in applied mechanics and engineering*, vol. **194**, pp. 4135–4195, 2005.

- Hutzenthaler, M., Jentzen, A., Kruse, T., and Nguyen, T.A., A Proof That Rectified Deep Neural Networks Overcome the Curse of Dimensionality in the Numerical Approximation of Semilinear Heat Equations, *SN partial differential equations and applications*, vol. **1**, no. 2, pp. 1–34, 2020.
- Ion, I.G., Bontinck, Z., Loukrezis, D., Römer, U., Lass, O., Ulbrich, S., Schöps, S., and De Gersem, H., Robust Shape Optimization of Electric Devices based on Deterministic Optimization Methods and Finite-Element Analysis with Affine Parametrization and Design Elements, *Electrical Engineering*, vol. **100**, no. 4, pp. 2635–2647, 2018.
- Jagtap, A.D. and Karniadakis, G.E., Extended Physics-Informed Neural Networks (XPINNs): A Generalized Space-Time Domain Decomposition Based Deep Learning Framework for Nonlinear Partial Differential Equations, *Communications in Computational Physics*, vol. **28**, no. 5, pp. 2002–2041, 2020.
- Jagtap, A.D., Kawaguchi, K., and Em Karniadakis, G., Locally Adaptive Activation Functions with Slope Recovery for Deep and Physics-Informed Neural Networks, *Proceedings of the Royal Society A*, vol. **476**, no. 2239, p. 20200334, 2020a.
- Jagtap, A.D., Kawaguchi, K., and Karniadakis, G.E., Adaptive Activation Functions Accelerate Convergence in Deep and Physics-Informed Neural Networks, *Journal of Computational Physics*, vol. **404**, p. 109136, 2020b.
- Jagtap, A.D., Kharazmi, E., and Karniadakis, G.E., Conservative Physics-Informed Neural Networks on Discrete Domains for Conservation Laws: Applications to Forward and Inverse Problems, *Computer Methods in Applied Mechanics and Engineering*, vol. **365**, p. 113028, 2020c.
- Jouppi, N., Young, C., Patil, N., and Patterson, D., Motivation for and Evaluation of the First Tensor Processing Unit, *IEEE Micro*, vol. **38**, no. 3, pp. 10–19, 2018.
- Kharazmi, E., Zhang, Z., and Karniadakis, G.E., Hp-VPINNs: Variational Physics-Informed Neural Networks with Domain Decomposition, *Computer Methods in Applied Mechanics and Engineering*, vol. **374**, p. 113547, 2021.
- Khodayi-Mehr, R. and Zavlanos, M., VarNet: Variational Neural Networks for the Solution of Partial Differential Equations, *Learning for Dynamics and Control*, PMLR, pp. 298–307, 2020.
- Kim, J., Lee, K., Lee, D., Jhin, S.Y., and Park, N., DPM: A Novel Training Method for Physics-Informed Neural Networks in Extrapolation, *Proceedings of the AAAI Conference on Artificial Intelligence*, Vol. 35, pp. 8146–8154, 2021.
- Kingma, D.P. and Ba, J., Adam: A Method for Stochastic Optimization, *3rd International Conference for Learning Representations*, San Diego, pp. 1–10, 2015.
- Kleiss, S.K. and Tomar, S.K., 2015. Two-sided robust and sharp a posteriori error estimates in isogeometric discretization of elliptic problems. *Isogeometric Analysis and Applications 2014*. Springer, pp. 231–246.
- Klenke, A., *Wahrscheinlichkeitstheorie*, Springer, 2006.
- Lagaris, I., Likas, A., and Fotiadis, D., Artificial Neural Networks for Solving Ordinary and Partial Differential Equations, *IEEE Transactions on Neural Networks*, vol. **9**, pp. 987–1000, 1998.
- Lagaris, I.E., Likas, A.C., and Papageorgiou, D.G., Neural-Network Methods for Boundary Value Problems with Irregular Boundaries, *IEEE Transactions on Neural Networks*, vol. **11**, no. 5, pp. 1041–1049, 2000.
- Langer, U., Mantzaflaris, A., Moore, S.E., and Touloupoulos, I., 2015. Multipatch discontinuous galerkin isogeometric analysis. *Isogeometric Analysis and Applications 2014*. Springer, pp. 1–32.
- LeCun, Y., 1.1 Deep Learning Hardware: Past, Present, and Future, *2019 IEEE International Solid-State Circuits Conference-(ISSCC)*, IEEE, pp. 12–19, 2019.
- Lee, H. and Kang, I.S., Neural Algorithm for Solving Differential Equations, *Journal of Computational Physics*, vol. **91**, no. 1, pp. 110–131, 1990.
- Lee, K., Trask, N.A., Patel, R.G., Gulian, M.A., and Cyr, E.C., Partition of Unity Networks: Deep *hp*-Approximation, *arXiv preprint arXiv:2101.11256*, 2021.
- Lemieux, C., *Monte Carlo and Quasi-Monte Carlo Sampling*, Springer Science & Business Media, 2009.

- Li, K., Tang, K., Wu, T., and Liao, Q., D3M: A Deep Domain Decomposition Method for Partial Differential Equations, *IEEE Access*, vol. **8**, pp. 5283–5294, 2019.
- Li, W., Xiang, X., and Xu, Y., Deep Domain Decomposition Method: Elliptic Problems, *Mathematical and Scientific Machine Learning*, PMLR, pp. 269–286, 2020.
- Liao, Y. and Ming, P., Deep Nitsche Method: Deep Ritz Method with Essential Boundary Conditions, *Communications in Computational Physics*, vol. **29**, no. 5, pp. 1365–1384, 2021.
- Long, Z., Lu, Y., and Dong, B., PDE-Net 2.0: Learning PDEs from Data with a Numeric-Symbolic Hybrid Deep Network, *Journal of Computational Physics*, vol. **399**, p. 108925, 2019.
- Long, Z., Lu, Y., Ma, X., and Dong, B., PDE-Net: Learning PDEs from Data, *International Conference on Machine Learning*, pp. 3214–3222, 2018.
- Lu, L., Meng, X., Mao, Z., and Karniadakis, G.E., DeepXDE: A Deep Learning Library for Solving Differential Equations, *SIAM Review*, vol. **63**, no. 1, pp. 208–228, 2021.
- Mall, S. and Chakraverty, S., Application of Legendre Neural Network for Solving Ordinary Differential Equations, *Applied Soft Computing*, vol. **43**, pp. 347–356, 2016.
- Markidis, S., The Old and the New: Can Physics-Informed Deep-Learning Replace Traditional Linear Solvers?, *Frontiers in Big Data*, p. 92, 2021.
- McFall, K.S. and Mahan, J.R., Artificial Neural Network Method for Solution of Boundary Value Problems With Exact Satisfaction of Arbitrary Boundary Conditions, *IEEE Transactions on Neural Networks*, vol. **20**, pp. 1221–1233, 2009.
- Meade Jr, A.J. and Fernandez, A.A., The Numerical Solution of Linear Ordinary Differential Equations by Feedforward Neural Networks, *Mathematical and Computer Modelling*, vol. **19**, no. 12, pp. 1–25, 1994.
- Merkel, M., Gangl, P., and Schöps, S., Shape Optimization of Rotating Electric Machines Using Isogeometric Analysis, *IEEE Transactions on Energy Conversion*, vol. **36**, no. 4, pp. 2683–2690, 2021.
- Pascanu, R., Mikolov, T., and Bengio, Y., On the Difficulty of Training Recurrent Neural Networks, *International conference on machine learning*, pp. 1310–1318, 2013.
- Paszke, A., Gross, S., Chintala, S., Chanan, G., Yang, E., DeVito, Z., Lin, Z., Desmaison, A., Antiga, L., and Lerer, A., Automatic Differentiation in Pytorch, 2017.
- Piegl, L. and Tiller, W., *The NURBS Book*, Springer Science & Business Media, 1996.
- Raissi, M., Perdikaris, P., and Karniadakis, G.E., Physics-Informed Neural Networks: A Deep Learning Framework for Solving Forward and Inverse Problems Involving Nonlinear Partial Differential Equations, *Journal of Computational Physics*, vol. **378**, pp. 686–707, 2019.
- Shin, Y., Darbon, J., and Em Karniadakis, G., On the Convergence of Physics Informed Neural Networks for Linear Second-Order Elliptic and Parabolic Type PDEs, *Communications in Computational Physics*, vol. **28**, no. 5, pp. 2042–2074, 2020.
- Sirignano, J. and Spiliopoulos, K., DGM: A Deep Learning Algorithm for Solving Partial Differential Equations, *Journal of Computational Physics*, vol. **375**, pp. 1339 – 1364, 2018.
URL <http://www.sciencedirect.com/science/article/pii/S0021999118305527>
- Strang, G. and Fix, G., *An Analysis of the Finite Element Method*, Wellesley-Cambridge Press, 1988.
URL <https://books.google.de/books?id=xZsMbyJYI-AC>
- Tokdar, S.T. and Kass, R.E., Importance Sampling: a Review, *Wiley Interdisciplinary Reviews: Computational Statistics*, vol. **2**, no. 1, pp. 54–60, 2010.
- Trask, N., Gulian, M., Huang, A., and Lee, K., Probabilistic Partition of Unity Networks: Clustering based Deep Approximation, *arXiv preprint arXiv:2107.03066*, 2021.
- Wang, S., Teng, Y., and Perdikaris, P., Understanding and Mitigating Gradient Flow Pathologies in Physics-Informed Neural Networks, *SIAM Journal on Scientific Computing*, vol. **43**, no. 5, pp. A3055–A3081, 2021.

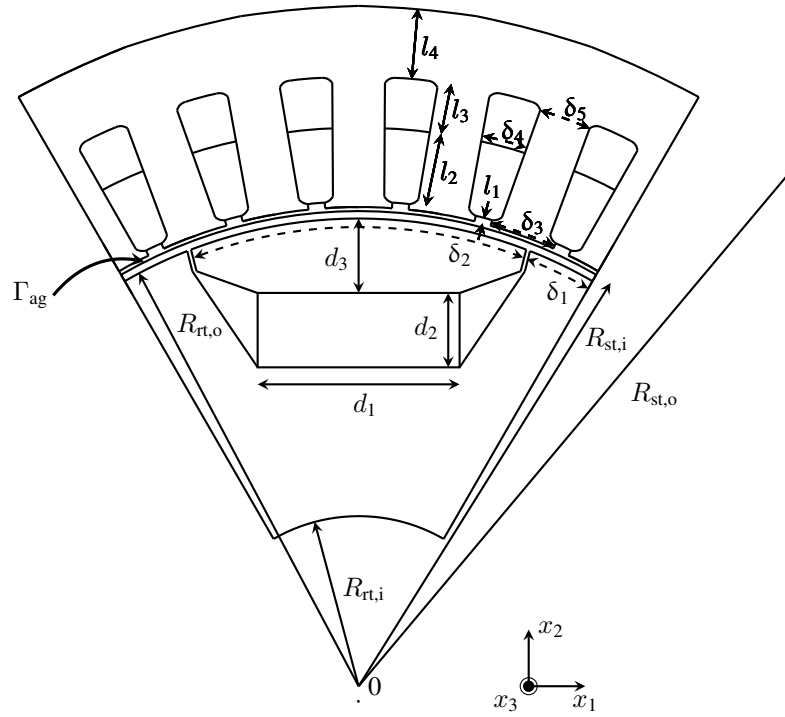


FIG. A1: One-sixth of the PMSM's geometry, along with its geometric parameters.

Yadav, N., Yadav, A., Kumar, M., , *An Introduction to Neural Network Methods for Differential Equations*, Springer, 2015.

APPENDIX A. GEOMETRICAL AND MATERIAL PARAMETERS OF THE PMSM

Description	Symbol	Value	Units
Inner rotor radius	$R_{rt,i}$	16	mm
Outer rotor radius	$R_{rt,o}$	44	mm
Radius of Γ_{ag}	R_{ag}	44.7	mm
Magnet width	d_1	19	mm
Magnet height	d_2	7	mm
Depth of magnet in rotor	d_3	7	mm
Inner stator radius	$R_{st,i}$	45	mm
Outer stator radius	$R_{st,o}$	67.5	mm
	δ_1	8.5	°
	δ_2	42	°
	δ_3	7	°
	δ_4	5.7	°
	δ_5	4	°
	l_1	0.6	mm
	l_2	5.4	mm
	l_3	5	mm
	l_4	8.2	mm

TABLE A1: Geometrical parameters of the PMSM, as depicted in figure A1.

Description	Symbol	Value	Units
Relative reluctivity of iron	ν_{Fe}	1/500	–
Relative reluctivity of copper	ν_{Cu}	1	–
Relative reluctivity of PM	ν_{PM}	1/1.05	–
Remanent magnetic field of PM	B_r	0.94	T

TABLE A2: Material parameters of the PMSM.